

Asymptotic behavior of a retracting two-dimensional fluid sheet

Leonardo Gordillo, Gilou Agbaglah, Laurent Duchemin, and Christophe Josserand

Citation: *Phys. Fluids* **23**, 122101 (2011); doi: 10.1063/1.3663577

View online: <http://dx.doi.org/10.1063/1.3663577>

View Table of Contents: <http://pof.aip.org/resource/1/PHFLE6/v23/i12>

Published by the [American Institute of Physics](#).

Related Articles

Maximum speed of dewetting on a fiber
Phys. Fluids **23**, 112103 (2011)

Optical interference effect on pattern formation in thin liquid films on solid substrates induced by irradiative heating
Phys. Fluids **23**, 112102 (2011)

Quasistatic computer simulations of shear behavior of water nanoconfined between mica surfaces
J. Chem. Phys. **135**, 174704 (2011)

Features of the rupture of free hanging liquid film under the action of a thermal load
Phys. Fluids **23**, 102106 (2011)

Regularized shock solutions in coating flows with small surface tension
Phys. Fluids **23**, 093103 (2011)

Additional information on *Phys. Fluids*

Journal Homepage: <http://pof.aip.org/>

Journal Information: http://pof.aip.org/about/about_the_journal

Top downloads: http://pof.aip.org/features/most_downloaded

Information for Authors: <http://pof.aip.org/authors>

ADVERTISEMENT



**Running in Circles Looking
for the Best Science Job?**

Search hundreds of exciting
new jobs each month!

<http://careers.physicstoday.org/jobs>

physicstodayJOBS



Asymptotic behavior of a retracting two-dimensional fluid sheet

Leonardo Gordillo,¹ Gilou Agbaglah,² Laurent Duchemin,³ and Christophe Josserand²

¹*Departamento de Física, Facultad de Ciencias Físicas y Matemáticas, Universidad de Chile, Casilla 487-3, Santiago, Chile*

²*Institut Jean Le Rond D'Alembert, CNRS & UPMC (Univ. Paris VI) UMR 7190 Case 162, 4 place Jussieu, F-75252 Paris Cédex 05, France*

³*IRPHE, Université d'Aix-Marseille I & II-CNRS 49 rue Joliot-Curie, BP 146, 13384 Marseille CEDEX, France*

(Received 3 August 2011; accepted 3 November 2011; published online 7 December 2011)

Two-dimensional (2D) capillary retraction of a viscous liquid film is studied using numerical and analytical approaches for both diphasic and free surface flows. Full 2D Navier-Stokes equations are integrated numerically for the diphasic case, while one-dimensional (1D) free surface model equations are used for free surface flows. No pinch-off is observed in the film in any of these cases. By means of an asymptotic matching method on the 1D model, we derive an analytical expansion of the film profile for large times. Our analysis shows that three regions with different timescales can be identified during retraction: the rim, the film, and an intermediate domain connecting these two regions. The numerical simulations performed on both models show good agreement with the analytical results. Finally, we report the appearance of an instability in the diphasic retracting film for small Ohnesorge number. We understand this as a Kelvin-Helmholtz instability arising due to the formation of a shear layer in the neck region during the retraction. © 2011 American Institute of Physics. [doi:10.1063/1.3663577]

I. INTRODUCTION

A thin liquid sheet retracts due to the action of the surface tension forming a growing rim at its retracting end as it recedes. In 1959, Taylor and Cullick^{1,2} found simultaneously that the retracting speed of a liquid film of uniform thickness $2e$ converges to a constant velocity U_{TC} given by the balance between inertia and surface tension

$$U_{TC} = \sqrt{\frac{\gamma}{\rho e}},$$

where γ is the surface tension and ρ is the liquid density. Numerical simulations (cf. Sec. II) show that, asymptotically, the geometry of the rim tends to a circular shape, whose radius evolves as the square-root of time¹⁻³ as illustrated in Figure 1.

Retraction dynamics is a crucial topic in many interface dynamics problems such as curtain coating,⁴ atomization,^{5,6} and drop impact dynamics.⁷ In fact, many liquid sheet instabilities commonly observed in nature are triggered by edge retraction. Such a mechanism is reported in liquid curtains, where transverse instabilities generated by retracting edges can exhibit spatio-temporal chaos.^{8,9} In liquid jets, disintegration of thin films leads to the formation of small droplets and full atomization.¹⁰ In drop impact, the splashing and the corona instability are linked to the dynamics of a free liquid edge.¹¹⁻¹³

Hence, a further analysis which goes beyond the classical Taylor-Cullick theory is of utmost importance for understanding film motion. The quasi-stationary Taylor-Cullick model is based on non-local mass and momentum conservation without considering viscosity at all. In contrast, transient dynamics and viscous effects can highly change the retraction

behavior.¹⁴⁻¹⁸ For instance, the liquid viscosity affects the timescale of the transitory regime leading to the Taylor-Cullick velocity¹⁷ and it also influences drastically the transverse instability of the film.^{12,19,20} The film profile dependence on the liquid viscosity in the quasi-stationary regime at constant velocity is even more remarkable, as it has already been seen in experiments and numerical simulations.¹⁴⁻¹⁷ For instance, there is experimental evidence that a very viscous film does not form any rim during retraction and that the film apparently thickens as it retracts.^{14,15} Actually, numerical simulations of the thin film equations have shown that in this case, a very large retracting edge forms, which is thicker than the film and the experimental film length.¹⁶ On the other hand, when the viscous effects are small enough, a thin neck connects the rim to the film of constant thickness. In that situation, one can ask whether this neck can lead to the two-dimensional (2D) break-up of the film in the inviscid limit for a large rim radius as postulated by Song and Tryggvason.²¹

Therefore, the classical picture of a circular rim retracting into a film of constant thickness has to be revised. In this article, we investigate numerically and analytically the 2D film profile evolution in the large time limit, i.e., when the rim radius is much larger than the film thickness, so that the film can be expanded into a quasi-stationary regime approximation. In Sec. II, we present the problem describing and comparing the two numerical methods used to model the film dynamics, i.e., integration of the Navier-Stokes equation for the full system (liquid film and surrounding gas), and simulation of the one-dimensional (1D) system of equations obtained for thin films using the free surface boundary conditions and lubrication approximation. In Sec. III, we present the film dynamics within the 1D model in the

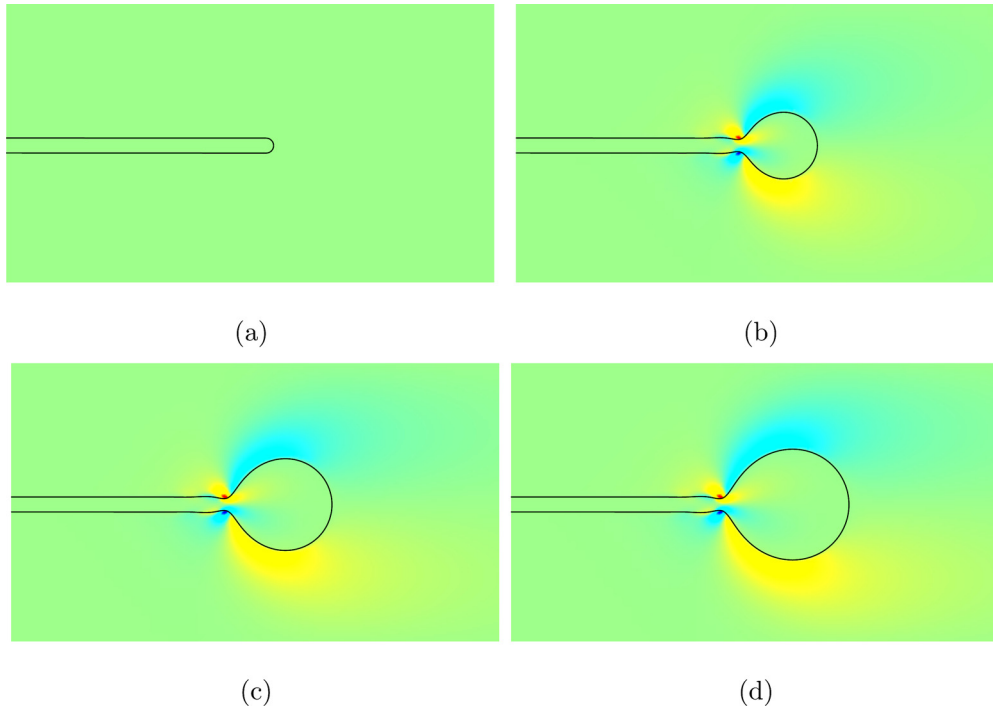


FIG. 1. (Color online) Evolution of the sheet interface and vorticity field for $Z=0.14$ at four different dimensionless times: (a) $t^*=0$, (b) $t^*=10$, (c) $t^*=20$, and (d) $t^*=30$. The incompressible Navier-Stokes equations are solved for both fluids using a VOF method in GERRIS.²²

quasi-stationary approximation. A mathematical analysis of the 1D system of equations for large times shows that the time asymptotic solution can be separated into three different regions—film, neck and rim—with different length and time scales. These regions can then be matched together in the spatial domain in order to build a whole domain solution. The details of the calculations can be found in Appendices A and B. We would like to emphasize that obtaining such a quasi-analytical solution of the 2D film retraction opens the way to improving the 3D linear stability analysis of liquid films, by taking into account the film profile shape in a more accurate way. Finally, the comparison between asymptotic solutions and numerics is discussed in Sec. IV.

II. DYNAMICS OF THE RETRACTING FILM

A. Fluids equations

We consider the two dimensional dynamics of a thin film of initial uniform thickness $2e$ of a liquid in the presence of a surrounding gas. The densities and dynamical viscosities of the liquid and the gas are noted as (ρ_L, ρ_G) and (μ_L, μ_G) , respectively. Both fluids can be considered as incompressible, thus, the dynamics is governed by the 2-D incompressible Navier-Stokes equations

$$\rho(\partial_t \mathbf{u} + \mathbf{u} \cdot \nabla \mathbf{u}) = -\nabla p + \mu \Delta \mathbf{u} + \gamma \kappa \delta_s \mathbf{n}, \quad (1)$$

$$\nabla \cdot \mathbf{u} = 0, \quad (2)$$

where the velocity and pressure fields are noted $\mathbf{u} = u\mathbf{e}_x + v\mathbf{e}_y$ and p , γ being the liquid-gas surface tension. Capillary forces are modeled by introducing the Dirac delta function δ_s at the interface, with \mathbf{n} and κ denoting the local normal direction and the local curvature of the interface, respectively.

Consequently, in this formulation, ρ and μ are discontinuous scalar fields that account for the densities and viscosities of each fluid. If we define the capillary time $\tau = \sqrt{\rho_L e^3 / \gamma}$, the dynamics can then be rewritten in terms of dimensionless variables

$$\tilde{\rho}(\partial_t \mathbf{u} + \mathbf{u} \cdot \nabla \mathbf{u}) = -\nabla p + Z \tilde{\mu} \Delta \mathbf{u} + \kappa \delta_s \mathbf{n}, \quad (3)$$

$$\nabla \cdot \mathbf{u} = 0. \quad (4)$$

The length, time, velocity, pressure, density, and viscosity have been rescaled by e , τ , $U_{TC} = \sqrt{\gamma / \rho_L e}$, γ/e , ρ_L , and μ_L , respectively. Besides the density and viscosity ratios, the dynamics depends only on one dimensionless number, the Ohnesorge number Z , which compares viscous and capillary effects

$$Z = \frac{\mu_L}{\sqrt{\rho_L \gamma e}}.$$

The dimensionless density $\tilde{\rho}$ and viscosity $\tilde{\mu}$ are both 1 in the liquid phase and ρ_G/ρ_L and μ_G/μ_L , respectively, in the gas phase. As a consequence, the case of free surface flow can be easily accounted for by considering $\rho_G = 0$ and $\mu_G = 0$.

B. Full numerical simulations

Numerical integration of the set of Eqs. (3) and (4) is performed using the GERRIS code,²² which uses a staggered-in-time discretisation of the volume-fraction/density and pressure. The interface was tracked using the volume of fluid method (VOF) and an adaptive mesh refinement based on quadtree decomposition (octree in 3D) is used. The combination of both techniques allows efficient computation of complex interfacial flows.^{23–25}

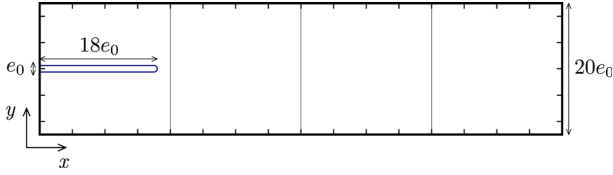


FIG. 2. (Color online) Spatial domain and initial condition for the retracting sheet numerical simulation. The domain consists of four square subdomains. The initial length of the sheet is $18e_0$ and the square subdomain length is $20e_0$.

As an initial condition, we considered a long free end liquid film of thickness $e_0 = 2e$ as illustrated in Figure 2. The simulations were performed in a comoving frame of reference that recedes at the Taylor-Cullick velocity. This was achieved by imposing Dirichlet boundary conditions for the velocity field on the left boundary and an outlet condition on the right side. On the other hand, the mesh refinement is controlled both by the interface position and the vorticity field, in order to maintain a good resolution around the interface as well as in the region where the vorticity becomes strong. We will consider later an air/water like system by setting the density and viscosity ratios to $\rho_L/\rho_G = 850$ and $\mu_L/\mu_G = 50$, respectively. The evolution of the film profile and the vorticity field is shown in Figure 1 for $Z = 0.14$. The surface tension pulls back the rim and, after a few units of dimensionless time, the rim reaches the Taylor-Cullick velocity U_{TC} , which corresponds to rest in the comoving frame. Then, a quasi-stationary regime sets up where the most of the dynamics consists of a slow increase of the rim size. We will refer to this asymptotic stage as the Taylor-Cullick regime. As a first approach, following the arguments of Taylor and Cullick,^{1,2,26} the rim can be considered circular (see Figure 3) and a simple mass balance equation for the rim gives the evolution of the rim radius $R(t)$,

$$2eU_{TC} = \frac{d}{dt} (\pi R(t)^2).$$

This equation can be easily integrated with our initial conditions and yields

$$R(t)^2 = \left(\frac{2}{\pi}\right)t + 1,$$

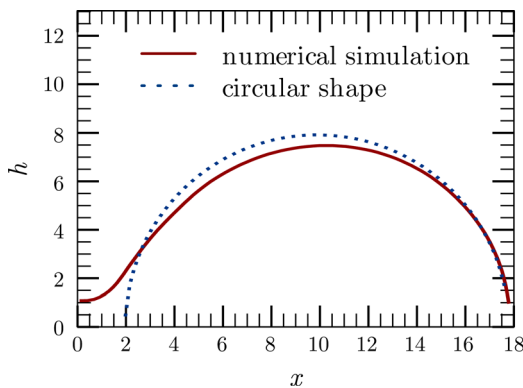


FIG. 3. (Color online) Fit between numerical rim for $Z = 0.14$ at $t = 20$ and circular shape, $(x - 0.199)^2 + y^2 = 0.025$

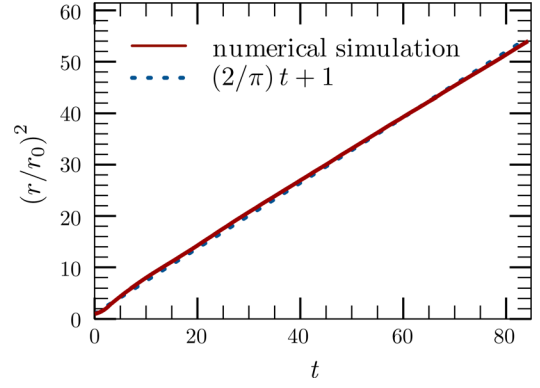


FIG. 4. (Color online) Time evolution of the rim radius extracted from the direct numerical simulation of the capillary film retraction. The linear law expected by the Taylor-Cullick regime is in very good agreement with the numerics.

in dimensionless units. This is in good agreement with the numerical results shown in Figure 4. However, we must note that this result relies on the rim being an approximately circular profile, a feature that depends strongly on the Ohnesorge number (see Figure 5). In particular, we observe a qualitative change in the film profile as the Ohnesorge varies. For viscous liquid, i.e., high Ohnesorge number, the film thickness decays monotonically in the upstream $-x$ direction. By contrast, for capillary driven flows, i.e., low Ohnesorge number, one can observe spatial oscillations, whose amplitude decreases with the distance to the rim. The profile behind the rim seems to be quite stable after convergence to the Taylor-Cullick velocity, at least for the first two cases ($Z = 0.7$ and $Z = 0.14$). Figure 5 also shows that for low Ohnesorge numbers, vorticity is mainly concentrated in strong curvature points, especially in the first minimum region behind the rim. Henceforth, we will refer to these regions as the neck of the film, following Song and Tryggvason.²¹

C. Thin film equation

When the effects of the surrounding gas can be neglected, the Navier-Stokes equations with free surface boundary conditions can be reduced to a set of coupled equations within the thin film approximations—or long wavelength limit, where horizontal variations can be considered much smaller than the vertical ones—as shown by Erneux and Davis.²⁷ The equations are written in terms of the local thickness $2h(x,t)$ and the parallel velocity of the flow $u(x,t)$, in dimensionless form

$$\partial_t h + \partial_x (hu) = 0, \quad (5)$$

$$\partial_t (hu) + \partial_x (hu^2) = \partial_x \left[4Zh\partial_x u + \int h\partial_x \kappa \, dx \right]. \quad (6)$$

This set of equations, obtained within the lubrication approximation, is valid both in a fixed reference frame or in a constant velocity moving frame. Equation (5) is derived from local mass conservation in the film while Eq. (6), written here in a conservative form, corresponds to the local

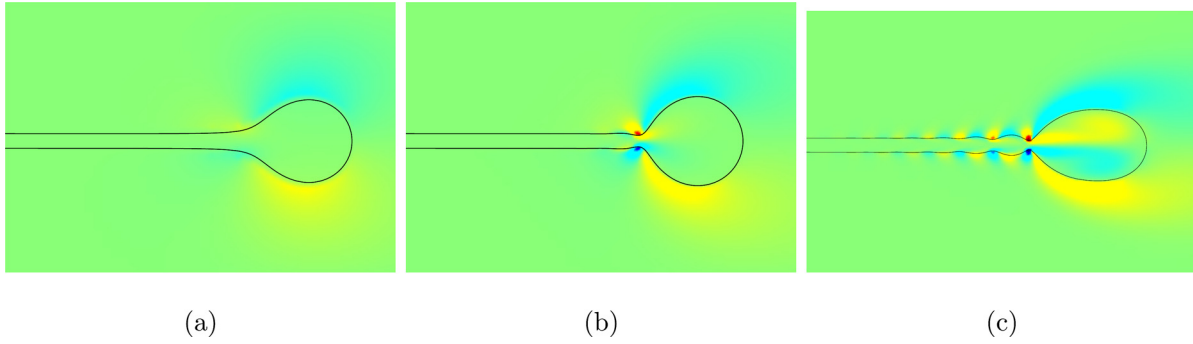


FIG. 5. (Color online) Sheet profile and vorticity field for three different Ohnesorge numbers at $t=20$: (a) $Z=0.7$, (b) $Z=0.14$, and (c) $Z=0.028$.

momentum balance. However, in order to cope with the tip of the rim, the surface-tension term has to be amended by using the complete curvature κ instead of its long wavelength limit $\kappa \approx \partial_{xx}h$. The integral associated with the surface tension term can then be expressed in a closed form

$$\int h \partial_x \kappa \, dx = \frac{h \partial_{xx}h + (\partial_x h)^2 + 1}{\sqrt{1 + (\partial_x h)^2}}.$$

This model has been able to reproduce successfully 2D film retraction when the film is semi-infinite.¹⁶ The set of Eqs. (5) and (6) is well-posed by adding consistent initial conditions. For the free retracting fluid sheet, this problem can also be seen as a kind of boundary value problem on a semi-infinite domain which evolves with time. In the Taylor-Cullick velocity moving frame the solutions satisfy a Dirichlet boundary condition far from the tip

$$\left. \begin{aligned} h(x, t) &= 1 \\ u(x, t) &= 1 \end{aligned} \right\} \text{ at } x = -\infty, \quad (7)$$

and a singular Cauchy boundary condition at the film tip,

$$\left. \begin{aligned} h(x, t) &= 0 \\ \partial_x h(x, t) &= -\infty \\ u(x, t) &= \dot{x}_0 \end{aligned} \right\} \text{ at } x = x_0(t). \quad (8)$$

The first boundary condition (7) comes from the unperturbed geometry far away from the rim and the influx velocity on the reference frame at which the rim does not recede. The second boundary condition (8) is imposed by the

kinematic condition at the tip and the symmetries of the problem.

Numerical simulation of these 1D Eqs. (5) and (6) can be performed using a finite difference method. Equations (5) and (6) are written in terms of u and $A = h^2$ and solved on a staggered grid. A numerical issue arising in these kinds of equations is that the computational domain shrinks in time. In order to avoid having a time-dependent grid, we mapped the domain into $[0, 1]$, rescaling x by the total length of the sheet $l(t)$. As a consequence, the boundary of the film is moving in this frame and one needs to write an equation for $\dot{l}(t)$. This equation simply says that the end point velocity, which can be extrapolated from the bulk velocity, equals $\dot{l}(t)$. The new set of equations reads

$$\partial_T A = -\frac{1}{l}(u - \dot{X})\partial_X A - \frac{2A}{l}\partial_X u, \quad (9)$$

$$\begin{aligned} \partial_T u &= -\frac{1}{l}(u - \dot{X})\partial_X u + \frac{4Z}{l^2 A^{1/2}}\partial_X (A^{1/2}\partial_X u) \\ &+ \frac{1}{l}\partial_X \kappa, \end{aligned} \quad (10)$$

$$\partial_T l = u(l(t), t), \quad (11)$$

where $X = x/l(t)$ and $T = t$.

A Runge-Kutta method is used together with centered finite difference formulas to solve this set of equations with $X \in [0, 1]$. The time evolution of the film retraction is shown in Figure 6 for the same Ohnesorge numbers as in Figure 5. The numerical solutions are robust when the domain size is such that the boundary is far enough from the spatial

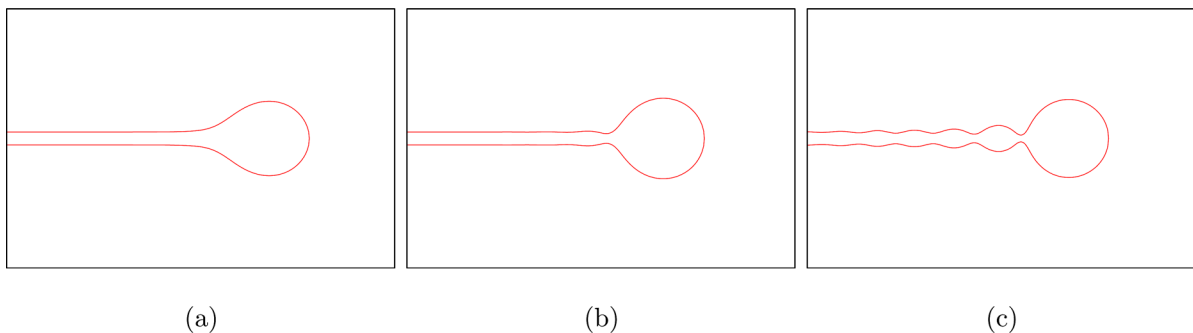


FIG. 6. (Color online) Sheet profile for three different Ohnesorge numbers at $t=20$, using the thin film approximation: (a) $Z=0.7$, (b) $Z=0.14$, and (c) $Z=0.028$.

oscillations behind the rim. Numerical convergence of the solution has been reached by changing the initial domain size ($l(0)$).

A good qualitative agreement is found between the two numerical methods. In particular, we observe that the film geometry changes similarly as the Ohnesorge number varies. Before we perform more quantitative comparisons, we investigate in Sec. III the main features of the solution of this model using analytic expansions in the asymptotic large time limit.

III. ASYMPTOTIC EXPANSION

We are thus interested in finding an asymptotic expansion for the thin film model of Eqs. (5) and (6) for large times. In this regime, the rim is already well formed so that we can consider that its radius is much larger than the film thickness ($R(t) \gg e$) and that its receding velocity is only slightly different from the Taylor-Cullick value. In such a limit, by choosing a proper set of length scales for x , y , and u , time derivatives can be neglected at least at the leading order, when other terms containing spatial derivative may become dominant. In order to obtain a solution valid in the whole domain at dominant and higher orders, we will analyze the nonlinear system given by Eqs. (5) and (6) at different self-similar scales. The existence of different length scales implies the appearance of several regions, which should be matched in space in order to generate a unique whole domain solution.

A. Far-field solution

We expect, as observed in our numerical simulations, that in the co-moving frame, the far-field flow remains unperturbed when the rim retracts. Thus, we pose solutions of the form

$$h_f(x, t) = h_f^{(0)}(z) + h_f^{(1)}(z, t), \quad (12)$$

$$u_f(x, t) = u_f^{(0)}(z) + u_f^{(1)}(z, t), \quad (13)$$

where $z \equiv x - x_f$ accounts for the translational invariance of the equations. The fields $h_f^{(1)}(z, t)$ and $u_f^{(1)}(z, t)$ are supposed to be small corrections of the dominant terms. Replacement of the *Ansatz* (12) and (13) into Eqs. (5) and (6), yields at zeroth order

$$\partial_z(hu) = 0, \quad (14)$$

$$\partial_z(hu^2) = \partial_z \left[4Zh\partial_z u + \frac{h\partial_{zz}h + (\partial_z h)^2 + 1}{\sqrt{1 + (\partial_z h)^2}} \right]. \quad (15)$$

We have omitted subscripts and superscript symbols for simplifying notations. The first equation can be easily integrated using the boundary conditions at infinity (7). Furthermore, the momentum equation (15) can be integrated after substitution of u in terms of h , yielding

$$\frac{1 + 4Z\partial_z h}{h} = \frac{h\partial_{zz}h + (\partial_z h)^2 + 1}{\sqrt{1 + (\partial_z h)^2}}. \quad (16)$$

Because of the momentum balance between the inertial and the surface-tension term at $-\infty$ coming from the Taylor-Cullick frame of reference, the constant of integration of Eq. (15) given by boundary conditions at $-\infty$ is zero.

At $z \rightarrow -\infty$, $h_f^{(0)}(z)$ tends to unity and nonlinear terms can be suppressed. The equation then behaves as a second order linear differential equation. By expanding the solution in this limit, i.e., $h_f^{(0)}(z) = 1 + \epsilon e^{k \cdot z}$, we obtain $k = 2Z \pm \sqrt{4Z^2 - 1}$. We find thus that the decay length scales as $4Z$ for large Ohnesorge number and as $(2Z)^{-1}$ for low ones. Moreover, the solution presents spatial oscillations if $Z < Z_0 = 0.5$ with wavenumber $k_i = \sqrt{1 - 4Z^2}$ which converge to unity for small Ohnesorge numbers, in quantitative agreement with our numerical results.

Numerical integration of Eq. (16) reveals the appearance of two types of derivative singularities at finite z , corresponding to a positive and a negative infinite slope of the interface, respectively, as shown in Figure 7. In fact, such singularities appear because steady finite solutions of Eq. (5) and (6) cannot be supported in the whole domain. Indeed, they would violate mass conservation since there is a net flux of mass from infinity. The phase portrait of Eq. (16) shows as well the existence of a manifold that behaves as the separatrix between the two types of singular solutions. This separatrix plays a crucial role since it corresponds formally to an infinite mass rim, the only one that is consistent with the mass conservation for the steady film evolution. Therefore, in the large time asymptotic limit, the rim should match this separatrix at the leading order. This curve is well defined in the whole domain and its asymptotical behavior can be found by balancing the viscous and the surface-tension terms of Eq. (16). At leading order, the separatrix is quadratic and it can be expanded around $z \rightarrow \infty$,

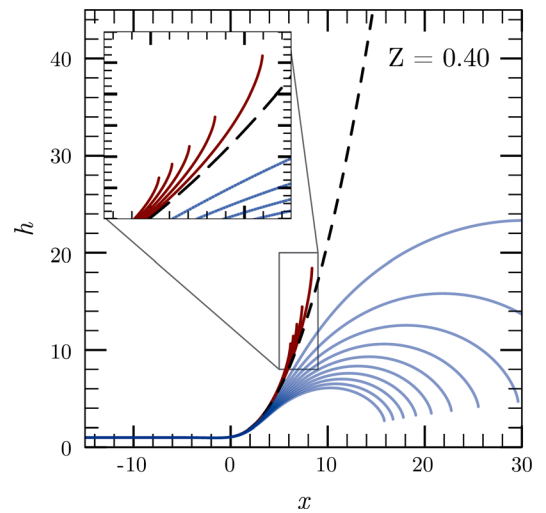


FIG. 7. (Color online) The two families of singular solutions of Eq. (16) can be obtained by choosing different initial conditions when performing numerical integration. Both families develop derivative singularities for finite x but differing sign diverging slopes: The upper left family for positive (red online) and the lower right family for negative (blue online). The separatrix (black dashed curve) is the unique function that can be defined in the whole domain.

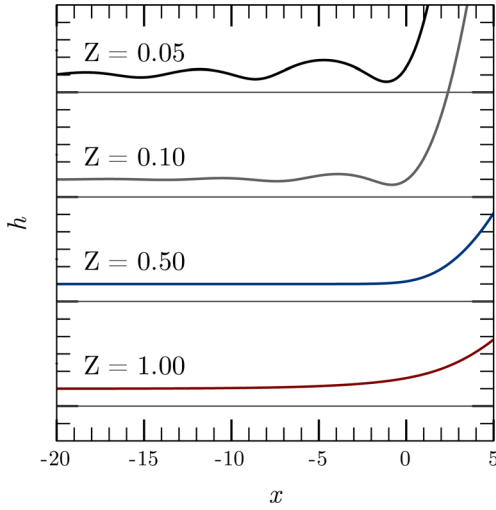


FIG. 8. (Color online) Steady *envelope* solutions arising from Eq. (16) for different Ohnesorge numbers. Equation (16) was integrated numerically in the $-x$ direction starting from a point near the separatrix for $x \gg 1$. Oscillations appear for $Z < 0.5$.

$$\lim_{z \rightarrow \infty} h_f^{(0)} = \left(\frac{3}{32Z} \right) z^2 - \frac{3}{28Z} z \ln z + \frac{3}{28Z} z + \frac{3}{98} \ln^2 z + \mathcal{O}(1). \quad (17)$$

The rise of this manifold is very important for calculations as it is the signature of the existence of another spatial region in which different expansions and scalings are required. In addition, we observe that this manifold exhibits a finite neck for small enough Ohnesorge number, i.e., $Z < 0.5$ (see Figure 8), which shows that no pinch-off can occur in the pure 2D dynamics of capillary retracting films. Indeed, even in the zero Ohnesorge number limit, we observe that the minimal film thickness tends to one half (see Figure 9). This can be proved by setting $Z=0$ in Eq. (16). The resulting equation can be integrated after multiplying it by $h^{-2} \partial_z h$, yielding

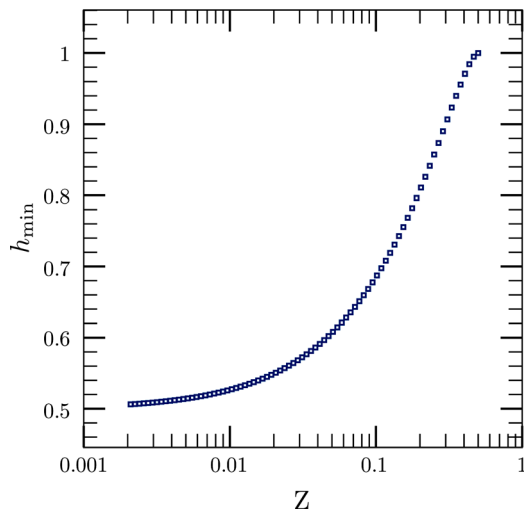


FIG. 9. (Color online) When the Ohnesorge number is $Z < \frac{1}{2}$, a neck is formed behind the rim. The figure shows the neck thickness dependence on the Ohnesorge number. Thickness values were obtained by numerical integration of Eq. (16), starting from a far point on the envelope (17).

$$\frac{1}{\sqrt{1 + (\partial_z h)^2}} = \frac{1}{2} h^{-1} - \frac{1}{2} a(a-2)h. \quad (18)$$

Depending on the choice of a , the constant of integration, the solutions can exist in an infinite domain or be restricted to a finite one. This can be understood through the analysis of the critical points of Eq. (18). For $0 < a < 2$, two critical points with opposite concavities can be found, giving rise to periodical solutions. In the case of $a > 2$, only one critical point has physical sense ($h > 0$) and due to its positive concavity, the solution develops an infinite slope for z finite. The critical case occurs when $a = 2$, with a solution given by

$$h^*(z) = \lim_{Z=0} h_0(z) = \frac{1}{2} \cosh(2z).$$

Ignoring the fact that the unique solution that can satisfy the boundary condition at $z \rightarrow -\infty$ occurs when $a = 1$ due to the loss of the dynamic term $\partial_z h$, the solution $h^*(z)$ can be regarded as the separatrix of Eq. (16) for $Z = 0$. Thus, its minimum defines the maximal lower bound for the neck thickness for any given $Z > 0$.

B. Rim solutions

It is imperative to look for a different kind of solution that supports a mass influx into the rim. Inspired by the numerical simulations and by the translational invariance of lubrication equations, we seek a quasi self-similar solution of the form

$$h_r(x, t) = R \left[h_r^{(0)}(\zeta) + h_r^{(1)}(\zeta, t) \right], \quad (19)$$

$$u_r(x, t) = R^{-1} \left[u_r^{(0)}(\zeta) + u_r^{(1)}(\zeta, t) \right], \quad (20)$$

where $\zeta \equiv R^{-1}(x - x_r) \equiv R^{-1}z$. The free spatial origin of the solution x_r has been introduced. The correction fields $h_r^{(1)}$, $u_r^{(1)}$ are small and $R \gg 1$ depend weakly on time. Theoretically, we can understand this scaling as a consequence of the appearance of a natural length scale in the rim given by the radius R . The fact that u_r scales with R^{-1} is related with the persistence of the flux quantity $hu = 1$ into this region as this quantity cannot depend on the R length scale.

At zeroth order, Eqs. (5) and (6) become, respectively (subscripts and superscripts omitted again),

$$RR\dot{h} - RR\dot{\zeta}\partial_\zeta h + \partial_\zeta(hu) = 0, \quad (21)$$

$$\partial_\zeta \left[\frac{h\partial_\zeta h + (\partial_\zeta h)^2 + 1}{\sqrt{1 + (\partial_\zeta h)^2}} \right] = 0. \quad (22)$$

The second equation is decoupled from the first one and also independent of the choice of R . By contrast, the continuity equation depends on the quantity $RR\dot{h}$. This equation gives physical and suitable solutions for our problem only if $RR\dot{h} = \mathcal{O}(1)$ in time, due to a least degeneracy argument.²⁸ This distinguished limit breaks the invariance $\zeta \rightarrow -\zeta$ and

allows solutions with a net flux at one side and no flux at the other one.

This system is also invariant under the two following set of transformations: $h \rightarrow R_0 h$, $\zeta \rightarrow \zeta/R_0$, $u \rightarrow R_0 u$ and $\zeta \rightarrow \zeta - \zeta_0$, $u \rightarrow u + RR_0 \zeta_0$. The second equation can in fact easily be integrated

$$h(\zeta) = \sqrt{R_0^2 - (\zeta - \zeta_0)^2}. \quad (23)$$

In terms of z and t , we can then write

$$h(z, t) = \sqrt{R^2 - (z - R)^2}, \quad (24)$$

where ζ_0 has been fixed to R_0 and the constant R_0 has been absorbed into R . This solution captures the dynamics observed in the growing rim and its circular shape. We remark that the power law dependence of $R(t)$ appears naturally, as $RR' = \mathcal{O}(1)$ implies $R \propto t^{\frac{1}{2}}$. Moreover, the result is independent of the Ohnesorge number because, at this order, the momentum is dominated by the surface tension term only. However, its validity is restricted to a finite domain $0 \leq z \leq 2R$. While the right side $z \sim 2R$ gives the correct description of the rim tip, it does not represent the physical solution on the left side when $z \rightarrow 0$ where the rim should connect to the film. The rim solution exhibits a singular behavior for $z \rightarrow 0$ that can be expanded

$$\lim_{z \rightarrow 0^+} h_r^{(0)}(z) = (2\rho)^{\frac{1}{2}} t^{\frac{1}{4} z^{\frac{1}{2}}} + \mathcal{O}\left(t^{-\frac{1}{4} z^{\frac{3}{2}}}\right). \quad (25)$$

Here, we have expressed our result in terms of ρ , where $\rho^2 = 2RR'$. The value of ρ can be found by imposing the boundary condition $hu = 1$ at $z = 0$, which is equivalent to enforcing the mass conservation. Straightforward calculations give

$$\rho = \sqrt{\frac{2}{\pi}}. \quad (26)$$

It can easily be seen that this rim solution cannot be matched to the film separatrix solution obtained above at the dominant order. Therefore, an intermediate region with a different self-similar scaling is required in order to match the two regions.

C. Intermediate region

The intermediate region will have to match for $z \rightarrow +\infty$ with the rim solution (that scales in the intermediate region like $t^{\frac{1}{2} z^{\frac{1}{2}}}$) and for $z \rightarrow 0$ with the separatrix (that scales there like z^2). We look for self-similar solutions of the form $h(z, t) = t^\alpha f(\frac{z}{t^\beta})$ that meet the time dependence of the matching, that is, $\alpha - \frac{1}{2}\beta = \frac{1}{4}$ and $\alpha - 2\beta = 0$. Hence, the unique self-similar scaling, which allows a matching between the far-field and the rim solutions, is

$$h_m(x, t) = t^{+\frac{1}{3}} \left[h_m^{(0)}(\xi) + h_m^{(1)}(\xi, t) \right], \quad (27)$$

$$u_m(x, t) = t^{-\frac{1}{3}} \left[u_{m0}^{(0)}(\xi) + u_m^{(1)}(\xi, t) \right], \quad (28)$$

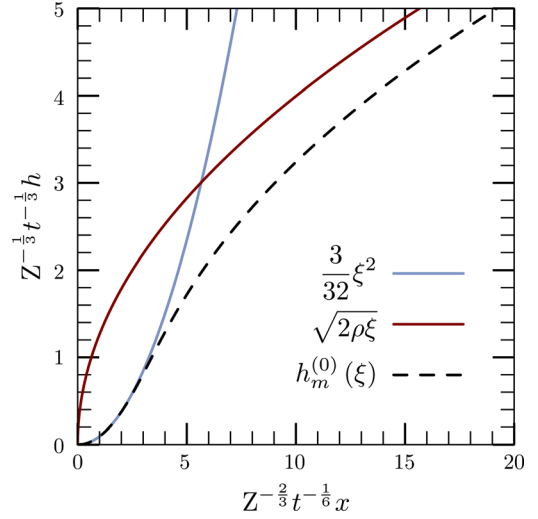


FIG. 10. (Color online) The solution of Eq. (31) (black dashed curve) unveils the shape of the intermediate region that links the steady solution with the growing rim. The asymptotic behavior when $x \rightarrow 0$ should coincide with the envelope of Eq. (16) for $x \rightarrow \infty$, while the behavior when $x \rightarrow \infty$ should match the solution of the growing rim when $t^{1/6} \ll x \ll t^{1/2}$, i.e., $\zeta \rightarrow 0$.

where $\zeta \equiv t^{-\frac{1}{6}}(x - x_m) \equiv t^{-\frac{1}{6}}z$ and $h_m^{(1)}$ and $u_m^{(1)}$ are correction terms. Indeed, the substitution of Eqs. (27) and (28) into Eqs. (5) and (6) gives at leading order the following set of equations (subscripts and superscripts have been omitted again),

$$\partial_\xi(hu) = 0, \quad (29)$$

$$\partial_\xi \left[\frac{h \partial_{\xi\xi} h + (\partial_\xi h)^2}{|\partial_\xi h|^3} \right] + 4Z \partial_\xi (h \partial_\xi u) = 0. \quad (30)$$

The continuity equation can be integrated using the boundary condition $hu = 1$ at $\xi \rightarrow 0$ as the flux should match the far-field incoming flow. Replacing u by means of h in the momentum balance equation gives us, as well, an equation which can be integrated again. Straightforward calculations provide

$$4Z \left(\frac{\partial_\xi h}{h} \right) = \frac{h \partial_{\xi\xi} h + (\partial_\xi h)^2}{|\partial_\xi h|^3}. \quad (31)$$

The constant of integration is zero because of the boundary conditions imposed at $\xi \rightarrow \infty$ and deduced from the matching with the rim solution. In this limit, the function must match the rim solution so $h_m^{(0)} \sim \xi^{\frac{1}{2}}$. Equation (31) is separable and it can be written as

$$\int h \left(\frac{8Z}{3} a^{-3} + \frac{8Z}{3} h^{-3} \right)^{\frac{1}{2}} dh = \xi - \xi_0,$$

where a is a constant of integration. The integral can be expressed in terms of hypergeometric functions after a change of variables. Then, the solution of the equations acquires a closed form

$$h(\xi) = a \Xi^{-1} \left[\left(\frac{3}{8Z} \right)^{\frac{1}{2}} \frac{\xi}{a^{\frac{1}{2}}} \right], \quad (32)$$

where $h(0) = 0$ has been imposed. Ξ^{-1} represents the inverse function of

$$\Xi(\eta) = 2\eta^{\frac{1}{2}} {}_2F_1\left(-\frac{1}{2}, \frac{1}{6}, \frac{7}{6}; -\eta^3\right), \quad (33)$$

or equivalently,

$$\Xi(\eta) = \frac{2^{\frac{2}{3}}\pi^2}{3[\Gamma(\frac{2}{3})]^3} + \frac{1}{2}\eta^2 {}_2F_1\left(-\frac{2}{3}, -\frac{1}{2}, \frac{1}{3}; -\eta^{-3}\right). \quad (34)$$

Both expressions have been included because the series of the hypergeometric function ${}_2F_1$ converges only inside the unitary circle. Therefore, each expression will be useful for matching the intermediate solution either with the far field or with the growing rim regions, respectively.

Expanding the function Ξ into a series of η , and inverting it in terms of Ξ , we get, at leading order, in terms of the physical variables,

$$\lim_{z \rightarrow \infty} h_m^{(0)}(z) = \left(\frac{3a^3}{2Z}\right)^{\frac{1}{4}} t^{\frac{1}{4}} z^{\frac{1}{2}} - A_0 \left(\frac{2Za^5}{3}\right)^{\frac{1}{4}} t^{\frac{5}{12}} z^{-\frac{1}{2}} + \left(\frac{Za^3}{6}\right)^{1/2} t^{\frac{1}{2}} z^{-1} + \mathcal{O}\left(z^{-\frac{3}{2}}\right), \quad (35)$$

$$\lim_{z \rightarrow 0} h_m^{(0)}(z) = \frac{3}{32Z} z^2 + \mathcal{O}(a^{-3} Z^{-4} t^{-1} z^8), \quad (36)$$

where $A_0 = \frac{2^{\frac{2}{3}}\pi^2}{3[\Gamma(\frac{2}{3})]^3}$ is the constant term of Eq. (34) (see Figure 10).

The previous results show that the intermediate region is always driven by viscous and surface-tension terms. Viscosity controls the *bridge* length, which scales with $Z^{\frac{2}{3}}$ (see Sec. III D for the a value) and expands in time following a $\frac{1}{6}$ th power law.

While the far-field region of the film can be easily identified in the interface as the unperturbed zone, the rim region is pointed out as the swelling zone close to the tip. In a similar way, the intermediate region can be recognized as the zone where the slope maximum takes place. This maximum is due to the change of curvature orientation required between the far-field and the rim region. In fact, the maximum slope of the interface at dominant order is given by

$$\max_x \left\{ \frac{\partial}{\partial x} h(x, t) \right\} = \mu Z^{-\frac{1}{3}} t^{\frac{1}{6}}. \quad (37)$$

The constant μ can be found directly from Eqs. (32) and (33). Figure 11 shows the results from 1D numerical simulations for the evolution of the film maximum slope for four different Ohnesorge numbers. The collapse of the four curves into a single one for large times is proof of the existence of this region. It has to be noticed, here, that because of the rapid variation of the profile near the neck, the lubrication approximation is in general not valid anymore in this region. This discrepancy is expected to be more relevant for small Ohnesorge numbers where inertia might become important.

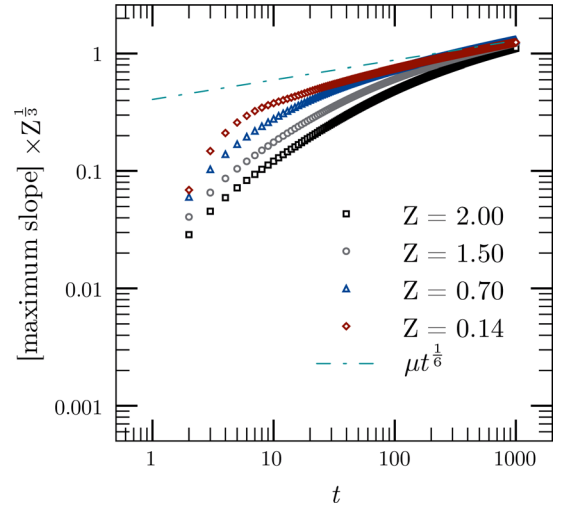


FIG. 11. (Color online) Maximum slope evolution from 1D numerical simulations for four different Ohnesorge numbers. The curves were rescaled by $Z^{\frac{1}{3}}$ following the analytical prediction. The asymptotic behavior is consistent with the asymptotic analysis of the 1D equations. The constant μ , which defines the vertical shift of the curve, was obtained from the asymptotic analysis and not by curve fitting.

D. Asymptotic matching

The three solutions that we have obtained can be matched when the free coefficients satisfy the following relations:

$$a = \left(\frac{16Z}{3\pi}\right)^{\frac{1}{3}}, \quad x_r = x_m = x_f = x_0,$$

as is shown in Figure 10. Indeed, as the lubrication equations are invariant under translations, we can freely choose $x_0 = 0$.

With the previous results, we can build a zeroth order non-uniform solution of lubrication equations (5) and (6) with proper boundary conditions (7) and (8),

$$h(x, t) = t^{\frac{1}{2}} h_r^{(0)}\left(xt^{-\frac{1}{2}}\right) + t^{\frac{1}{3}} h_m^{(0)}\left(xt^{-\frac{1}{6}}\right) + h_f^{(0)}(x) - \frac{3}{32Z} x^2 - (2\rho)^{\frac{1}{2}} t^{\frac{1}{4}} x^{\frac{1}{2}} + h_1(x, t), \quad (38)$$

where the perturbative field $h_1(x, t)$ comes from the sum of the perturbative fields $h_f^{(1)}$, $t^{\frac{1}{3}} h_m^{(1)}$, and $t^{\frac{1}{2}} h_r^{(1)}$. The function $h_r^{(0)}$ comes from Eq. (23) after substituting $\zeta_0 = -R_0$ and $R_0 = \rho$, while $h_m^{(0)}$ is defined by Eq. (32) after applying matching conditions. On the other hand, the function $h_f^{(0)}$ comes from the solution of Eq. (16) imposing (17).

Non-uniformity of the solution is due to the multiscale nature of the problem. A hierarchy of equations can be built up and the errors for each region follow different time scales since it corresponds to different spatial time-dependent scales. It is also important to notice that the convergence is very slow—the next term on the far-field solution behaves as $x \ln x$. This asymptotic tail adds an error of order $t^{\frac{1}{2}} \ln t$ into the rim region. Therefore, a higher-order analysis is strongly required.

E. Higher-order analysis

The calculation of higher-order terms calculations is complex. In the intermediate region, the integrals are very

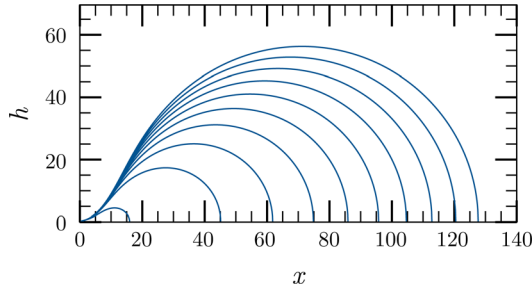


FIG. 12. (Color online) Asymptotic matching between the rim and the intermediate regions for $Z=1.0$ and $t=10^2$ to 80^2 time units. The rim swells as the flow is injected at $x=0$. The region near the origin barely changes during the motion.

hard to obtain analytically because they are related to non-tabulated functions. However, some results can still be deduced by numerical integration.

In Appendix A, we show how a hierarchy of linear equations for higher-order terms in each region can be found. Nonlinearities appear as forcing terms that couple each equation with lower-order terms. The tip position, which can also be expanded asymptotically in time, adds extra coupling terms in the equations.

The first non-trivial solution of the hierarchy that follows the zeroth order solution appears for $\mathcal{O}(t^{-1/3})$ corrections in the rim region. The inclusion of this correction suppresses an asymptotic tail error which adds an error that grew as $t^{\frac{1}{6}}$ in the rim region. In Figure 12, we plot the interface at different times for $Z=1.0$ using this higher-order term. The far-field region has not yet been included. Solutions are very similar to those obtained near the rim by S underhauf *et al.*¹⁷

It can be shown that the next term of the expansion in the rim region is $\mathcal{O}(t^{-1/2})$. At this level, the first correction for the tip position is obtained (see Appendix B for further

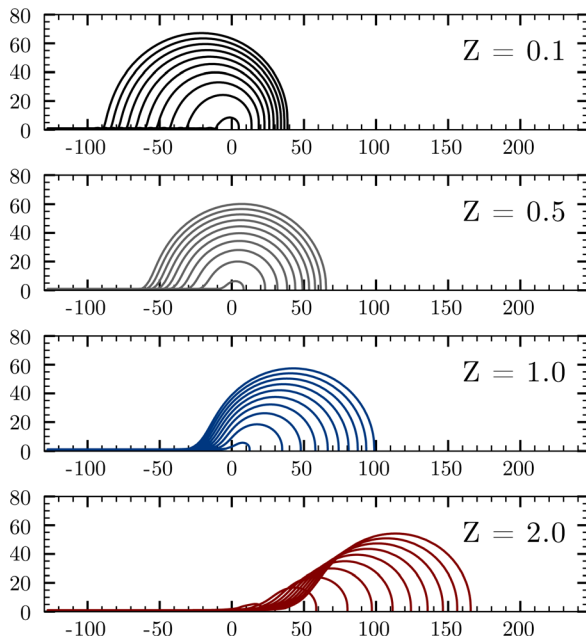


FIG. 13. (Color online) Asymptotic solutions for four different Ohnesorge numbers, $Z=0.1$, 0.5 , 1.0 , and 2.0 , in the comoving frame. The figures show the evolution between $t=10^2$ and $t=80^2$ in dimensionless time units.

details). In Figure 13, we show the asymptotic evolution of the interfaces obtained within this approach for several Ohnesorge numbers. In order to validate these solutions and, particularly, to estimate their accuracy, we require comparisons between these interface profiles and numerical simulations obtained with both the 1D model and with the full Navier-Stokes equations.

IV. COMPARISON AND DISCUSSION

Since the previous analytical results correspond to an expansion in the large time asymptotic regime, one expects the agreement—between numerical simulations and theory—to increase with time. Hence, we performed numerical simulations for both the full diphasic Navier-Stokes equations (3) and (4) and the 1D film equations (5) and (6) in order to compare the interface profiles with the asymptotic analysis developed in Sec. III for different times. We consider the two Ohnesorge numbers $Z=0.14$ and $Z=0.7$, investigating the two configurations with and without a neck, respectively. Figure 14 shows the different profiles at three different times showing a reasonable qualitative agreement between the numerics and the asymptotic analysis. In particular, the agreement is particularly good (quantitatively) between the asymptotic expansion of the 1D film equations and the numerics of the same equations, while some differences appear for the full Navier-Stokes equations. In addition, we want to emphasize that the asymptotic expansion limit, developed in Sec. III, gives a good analytical description of the film solution within the 1D long wavelength approximation. Moreover, the discrepancy between the 1D model and the full Navier-Stokes 2D equations can be explained both by the long-wave approximation of the 1D equations which is not valid for $|\partial_x h| \gg 0$ (i.e., in particular near the neck as discussed in Sec. II C), but also because of the free surface boundary conditions—Navier-Stokes equations account also for the gas dynamics.

In fact, we remark that in the diphasic case, a dynamical instability develops for large times and low Ohnesorge numbers, i.e., $Z \leq 0.018 \pm 0.003$, as was already reported by two of us.^{25,29} An example of such an instability is depicted in Figure 15(c). Such an instability is thus associated with the presence of the surrounding gas and it is related to the motion of a liquid rim within this gas.^{30,31} We argue here that the appearance of this destabilizing mechanism can be understood as the onset of a Kelvin-Helmholtz instability due to the strong shear layer created by the liquid retraction surrounded by the still gas. Indeed, when the gas is neglected, as is in the case for the 1D film equation for free surface flows, the development of the instability is completely suppressed in numerical simulations. The Kelvin-Helmholtz instability is in fact often invoked to explain atomization of liquid sheets, although in such cases only a small rim has been formed.^{5,10,32–35} The growth rate of the Kelvin-Helmholtz instability for a diphasic viscous flow without gravity is given by

$$\omega = \sqrt{\frac{\rho_L \rho_G}{(\rho_L + \rho_G)^2} k \Delta U - \nu k^2},$$

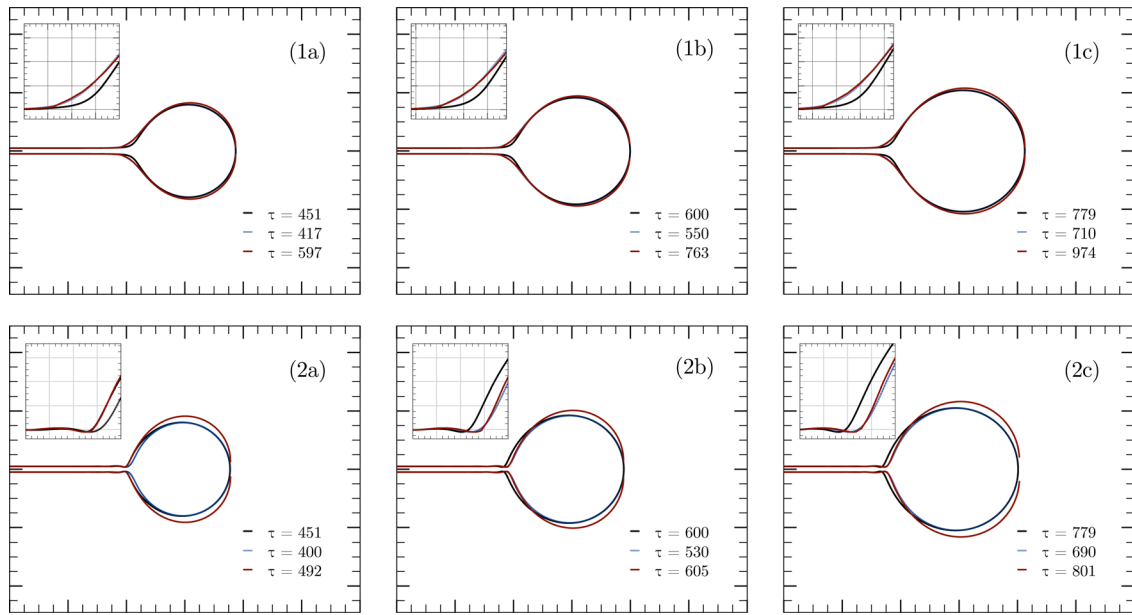


FIG. 14. (Color online) Comparison between the numerical simulations and the analytical approach of the evolution of the film thickness for two different Ohnesorge numbers: $Z = 0.7$ (1) and $Z = 0.14$ (2). The initial instability behind the rim and the rim curvature and size are practically the same in the three cases. From top to bottom in the legends, the curves correspond to: Navier-Stokes simulations (black line), thin film approximation, light gray line (blue online), and asymptotic expansion, gray line (red online). The insets show a zoom for the neck region. Simulation times are shown in the legend of each of the figures.

where k is the wavenumber ($k = 2\pi/\lambda$, with λ the wavelength), $\nu = \mu_L/\rho_L$ is the kinematic viscosity and $\Delta U \simeq U_{TC} = \sqrt{\gamma/\rho_L e}$. In the dimensionless units introduced above, we obtain

$$\omega = \sqrt{\frac{\rho_L \rho_G}{(\rho_L + \rho_G)^2} k^2 - Z k^2}.$$

The Kelvin-Helmholtz instability develops thus for $k < k_0 = \frac{1}{Z} \sqrt{\frac{\rho_L \rho_G}{(\rho_L + \rho_G)^2}}$, with the most unstable wave-number

$$k_{\max} = \frac{1}{2Z} \sqrt{\frac{\rho_L \rho_G}{(\rho_L + \rho_G)^2}}.$$

Taking $k_{\max} > k_i = \sqrt{1 - 4Z^2}$, the wavenumber of the spatial oscillation of the liquid film behind the rim, we obtain that the Kelvin-Helmholtz instability develops for

$$Z < Z_{\text{lim}} = \frac{1}{2} \sqrt{\frac{\rho_G}{\rho_L + \rho_G}}.$$

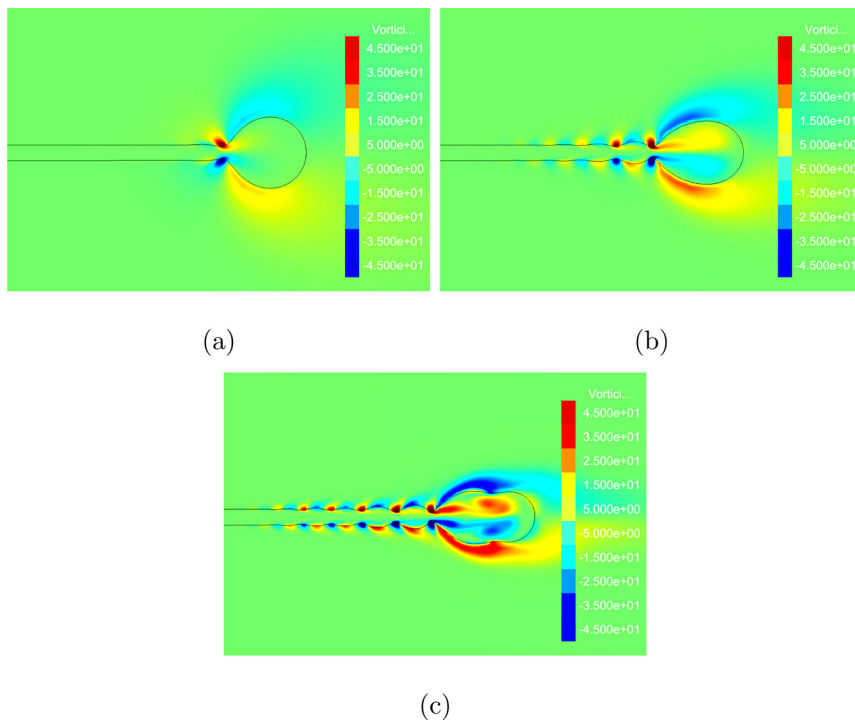


FIG. 15. (Color online) Sheet profile and vorticity field for three different Ohnesorge numbers at $t = 10.6$: (a) $Z = 0.14$, (b) $Z = 0.03$, and (c) $Z = 0.005$.

For the air-water system studied in our simulations, we obtain $Z_{lim} = 0.01714$ in very good agreement with our numerical estimate $Z \leq 0.018 \pm 0.003$. Finally, we would like to emphasize that even in these unstable cases, no sheet break-up is observed.

V. CONCLUSION

In this article, we have studied the 2D capillary retraction phenomenon of a viscous fluid film. Two different scenarios have been considered: a film surrounded by a viscous gas and a film with free surface boundary conditions. For the first case, we have solved numerically the diphasic full 2D Navier-Stokes equations (3) and (4) using GERRIS.²² For the second case, we have studied numerically and analytically the thin film 1D model given by Eqs. (5) and (6). An analytic expansion of the interface is obtained for this model using a matched asymptotic method in the large time regime. We report a good agreement between these analytical results and numerical simulation for the diphasic and the free surface flow cases. It is quite remarkable that our analysis shows that no pinch-off can occur in the 2D retraction. Moreover, the retracting film profile exhibits three well separated domains: the rim, the film, and an intermediate region, which connects them. The three regions have different length scalings for large times ($t^{1/2}$, 1, and $t^{1/6}$, respectively). Finally, we have consistently explained the destabilizing mechanism arising at low Ohnesorge number for diphasic systems in terms of a Kelvin-Helmholtz instability due to the shear between the liquid and the surrounding gas.

ACKNOWLEDGMENTS

We want to thank Stéphane Zaleski, Peter Mason, and colleagues from the Institut Jean Le Rond D'Alembert at UPMC for valuable discussions. L.G. and C.J. acknowledge the SCAT projet. L.G. also thanks the financial support of CONICYT through its project ACT 127 and C.J., the support of the Agence Nationale de la Recherche through its Grant DEFORMATION ANR-09-JCJC-0022-01 and of the Programme Émergence(s) of the Ville de Paris.

APPENDIX A: HIERARCHY OF EQUATIONS

Let us suppose that the corrective terms in Eqs. (12), (13), (19), (20), (27), and (28) can be expanded in a power series of t . A hierarchy of equations can then be written for each region. For each order, a linear differential operator acting on the n -th corrective term may be balanced with nonlinearities coming from lower-order terms. The free coefficients can then be fixed by matching leading terms with those coming from other regions.

For the rim region, the hierarchy adopts the form

$$\mathcal{L}_r h_r^{(n)} = X_r(\zeta) p_r^{(n)}(\zeta), \quad (\text{A1})$$

where $p_r^{(n)}$ depends on ζ through $h_r^{(i)}$ and $u_r^{(i)}$ with $i = 0 \dots (n-1)$ and

$$X_r(\zeta) = \frac{1}{h_r^{(0)}} \left[1 + \left(\partial_\zeta h_r^{(0)} \right)^2 \right]^{\frac{3}{2}}.$$

The kernel space of the linear operator is 2-D and can be built up using the solutions of the leading order equation found in Eq. (23) and is given by

$$\ker \mathcal{L}_r = \left\{ v_r = \frac{\rho - h_r^{(0)} \partial_\zeta h_r^{(0)}}{h_r^{(0)}}, \quad w_r = \frac{\rho + h_r^{(0)} \partial_\zeta h_r^{(0)}}{h_r^{(0)}} \right\}.$$

The non-homogeneous linear differential equation can be solved using the method of variation of parameters. The Wronskian of this set of solutions is

$$W_r(\zeta) = -2\rho h_r^{(0)-2}.$$

Thus the general solution of the ordinary differential equation (ODE) can be obtained from

$$\begin{aligned} h_r^{(n)}(\zeta) = & \frac{1}{2} \rho^2 \left(\int h_r^{(0)-2} w_r p_r^{(n)} d\zeta \right) v_r \\ & - \frac{1}{2} \rho^2 \left(\int h_r^{(0)-2} v_r p_r^{(n)} d\zeta \right) w_r \\ & - \rho P_r^{(n)} + A_r^{(n)} v_r + B_r^{(n)} w_r. \end{aligned}$$

It can be noticed that the solution space has an extra dimension given by a constant function associated with $P_r^{(n)}$. Anyway, this subspace does not interact directly, by means of integrals, with the lower order terms.

Similarly, one can find that for the intermediate region the hierarchy is

$$\mathcal{L}_m h_m^{(n)} = X_m(\xi) p_m^{(n)}(\xi), \quad (\text{A2})$$

where again $p_m^{(n)}$ depends on ξ through $h_m^{(i)}$ and $u_m^{(i)}$ with $i = 0 \dots (n-1)$ and

$$X_m(\xi) = \frac{1}{h_m^{(0)}} \left(\partial_\xi h_m^{(0)} \right)^3.$$

Now, the 2-D kernel can also be constructed from solutions of the zeroth order problem and can be chosen to be

$$\ker \mathcal{L}_m = \left\{ v_m = \frac{a}{\rho} \partial_\xi h_m^{(0)}, \quad w_m = \frac{1}{a} \left[h_m^{(0)} - \frac{1}{2} \xi \partial_\xi h_m^{(0)} \right] \right\}.$$

Straightforward calculations show that the Wronskian of the differential operator is

$$W_m(\xi) = \frac{3\pi}{4\rho} \left[h_m^{(0)} \right]^2 \left[\partial_\xi h_m^{(0)} \right]^4.$$

By taking these results into account, a closed solution can be found explicitly

$$\begin{aligned} h_m^{(n)}(\xi) = & -\frac{4\rho}{3\pi} \left(\int \left[h_m^{(0)3} \partial_\xi h_m^{(0)} \right]^{-1} w_m p_m^{(n)} d\xi \right) v_m \\ & + \frac{4\rho}{3\pi} \left(\int \left[h_m^{(0)3} \partial_\xi h_m^{(0)} \right]^{-1} v_m p_m^{(n)} d\xi \right) w_m \\ & + A_m^{(n)} v_m + B_m^{(n)} w_m + P_m^{(n)} \pi_m + Q_m^{(n)} \vartheta_m. \end{aligned}$$

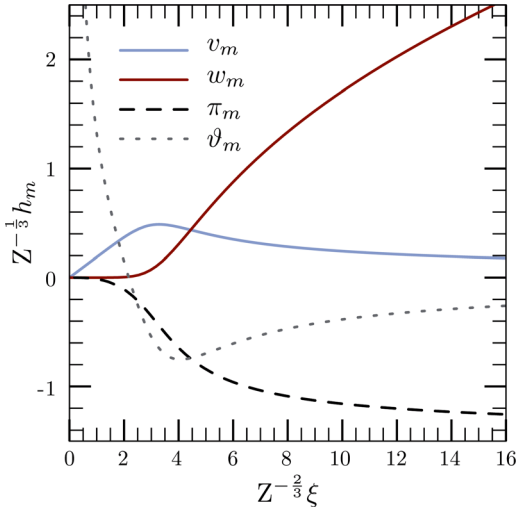


FIG. 16. (Color online) Solution space associated with the hierarchy linear operator of the intermediate region. The functions v_m and w_m are related to the translational and rim-size invariance, respectively.

The functions π_m and ϑ_m come from the constants of integration of the mass and momentum conservation equations. They also increase the solution space dimension by two, as was expected, without direct interaction with nonlinearities. The four functions of the solution space are plotted in Figure 16.

The boundary condition at the tip may also pose some problems because of the inherent divergence of the derivative. To avoid them, we promote the parameter x_0 as a weak function of time. As a result, the tip position will play some role in the hierarchy equations inducing extra terms for $p_r^{(n)}$ and $p_m^{(n)}$ in Eqs. (A1) and (A2).

The first non-trivial solution of the hierarchy that follows the zeroth order solution appears for $\mathcal{O}(t^{-1/3})$ corrections in the rim region. In this case, $p_r^{(1/3)} = 0$ in Eq. (A1) and this linear equation become homogeneous. Boundary conditions impose a solution of the form

$$h_r^{(1/3)}(\zeta) = B_r^{(1/3)} v_r(\zeta).$$

The constant $B_r^{(1/3)}$ can be obtained by matching the first term of $h_r^{(1/3)}$ around $\zeta=0$ with the second term of $h_m^{(0)}$ around $\zeta = \infty$ in the physical space. This yields

$$B_r^{(1/3)} = -A_0 \left(\frac{\pi Z a^5}{12} \right)^{\frac{1}{4}}.$$

APPENDIX B: HIGHER-ORDER TERMS

The next term of the expansion in the rim region is $\mathcal{O}(t^{-1/2})$. The effect of the tip motion has been added by expanding the tip position into a series, where $\dot{x}_0 t = -\sum c_\delta t^\delta$ with $\delta \leq \frac{1}{2}$. The existence of the first term, c_{12} which plays a role at this order, was suggested by Song and Tryggvason,²¹ who reported $\mathcal{O}(t^{-1/2})$ corrections in the neck velocity on their numerical simulations.

Thus, the forcing term in Eq. (A1) can be written as follows:

$$p_r^{(1/2)} = c_{1/2} h_r^{(0)} u_r^{(0)} - \frac{1}{2} \int \zeta \partial_\zeta (h_r^{(0)} u_r^{(0)}) d\zeta + h_r^{(0)} u_r^{(0)2} - 4Z h_r^{(0)} \partial_\zeta u_r^{(0)},$$

which shows that viscosity and inertia effects are incorporated at this order through the forcing term. Plugging the previous expression into Eq. (A1) and solving the integrals, one can find that the solution near $\zeta = 0$ behaves as

$$\lim_{\zeta \rightarrow 0} h_r^{(1/2)}(\zeta) = \frac{2Z}{3} \rho^{-1} \zeta^{-1} - \frac{1}{4\sqrt{2}} \rho^{\frac{1}{2}} \zeta^{-\frac{1}{2}} \ln \zeta + \left[\beta + \sqrt{2} \rho^{\frac{1}{2}} B_r^{(1/2)} \right] \zeta^{-\frac{1}{2}} + \gamma + \mathcal{O}\left(\zeta^{\frac{1}{2}} \ln \zeta\right), \quad (\text{B1})$$

where β and γ are constant terms that depend on Z and $c_{1/2}$. The coefficient $A_r^{(1/2)}$ was fixed to zero as the term associated with $w_r(\zeta)$ cannot fulfill the boundary condition when $\zeta = 2\rho$. When Eq. (B1) is written in the physical space, one finds that the first term matches the third term of expansion (35). By contrast, matching the second term needs further calculations. If any matching is possible, this term would correspond to the first of the $\mathcal{O}(t^{-1/6})$ corrections in the intermediate region. Moreover, the constant $B_r^{(1/2)}$ would be fixed by matching the third term of Eq. (B1) with the next term of the $\mathcal{O}(t^{-1/6})$ corrections.

After some straightforward calculations on this order of the intermediate region hierarchy, we find that the forcing term on Eq. (A2) is

$$p_m^{(1/6)} = \frac{1}{h_m^{(0)}},$$

which comes from inertial forces. If we replace the last expression in Eq. (A2), we can obtain the following order correction in terms of the variable η :

$$h_m^{(1/6)}(\zeta) = \frac{2\rho}{3a} [\Phi(\eta) v_m(\eta) - \Theta(\eta) w_m(\eta)] + A_m^{(1/6)} v_m(\eta) + B_m^{(1/6)} w_m(\eta)$$

which depends on $h_m^{(0)}$ through $\eta = h_m^{(0)}/a$. The terms containing $P_m^{(1/6)}$ and $Q_m^{(1/6)}$ constants have been omitted as it can be shown that the coefficients are equal to zero to ensure the matching.

The functions $\Phi(\eta)$ and $\Theta(\eta)$ are related to the integrals

$$\Phi(\eta) = \int_0^\eta t^{-3} (1 + t^{-3})^{\frac{1}{2}} dt, \\ \Theta(\eta) = \int_0^\eta t^{-2} (1 + t^{-3}) \left[t - \frac{1}{2} \frac{\Xi(t)}{\Xi'(t)} \right] dt,$$

which can be expanded analytically into series around $\eta = \infty$ and $\eta = 0^+$. Thus, we can calculate the asymptotic behavior of $h_m^{(1/6)}$ when $\eta \rightarrow \infty$,

$$\lim_{\eta \rightarrow \infty} h_m^{(1/6)}(\eta) = \left(\frac{3}{4} B_m^{(1/6)} - \frac{\sqrt{3}\pi\rho}{7aA_0} \right) \eta - \frac{\rho}{2a} \eta^{-1} \ln \eta + \left(A_m^{(1/6)} - \frac{A_0}{2} B_m^{(1/6)} + \frac{2\sqrt{3}\rho\pi}{21a} - \frac{\rho}{4a} \right) \eta^{-1} + \mathcal{O}(\eta^{-2}),$$

and the asymptotic behavior of $h_m^{(1/6)}$ when $\eta \rightarrow 0$,

$$\lim_{\eta \rightarrow 0} h_m^{(1/6)}(\eta) = -\frac{2\rho}{7a} \eta^{\frac{1}{2}} \ln \eta + \left(A_m^{(1/6)} - \frac{4\rho}{49a} \right) \eta^{\frac{1}{2}} + \mathcal{O}\left(\eta^{\frac{3}{2}} \ln \eta\right).$$

From the former of these expansions, we can already notice that the matching with the outer region is possible only if

$$B_m^{(1/6)} = \frac{4\pi\rho}{7\sqrt{3}aA_0}.$$

Furthermore, since we know the expansion of η in terms of ξ , the last result implies that

$$\lim_{\xi \rightarrow \infty} h_m^{(1/6)}(\xi) = -\frac{1}{4\sqrt{2}} \rho^{\frac{1}{2}} \xi^{-\frac{1}{2}} \ln \xi + \frac{1}{4\sqrt{2}} \rho^{\frac{1}{2}} \left[\frac{1}{2} \ln \frac{2Za}{3e^2} + \frac{8a}{3\rho} \delta + \frac{4a}{\rho} A_m^{(1/6)} \right] \xi^{-\frac{1}{2}} + \mathcal{O}(\xi^{-1}), \tag{B2}$$

$$\lim_{\xi \rightarrow 0} h_m^{(1/6)}(\xi) = -\frac{3}{28Z} \xi \ln \xi + \left[\frac{3}{56Z} \ln \frac{32Za}{3e^{2/7}} + \left(\frac{3}{32Za} \right)^{\frac{1}{2}} A_m^{(1/6)} \right] \xi + \mathcal{O}(\xi^2 \ln \xi). \tag{B3}$$

where δ is a constant depending on Z . When these expansions are written back into the physical plane, both dominant orders match, respectively, the secondary terms of expansions (17) and (B1). Besides, the constant coefficients $A_m^{(1/6)}$ and $B_r^{(1/2)}$ from Eqs. (B1)–(B3), which have not been fixed yet, should meet the following set of two linear equations:

$$\begin{aligned} \frac{3}{56Z} \ln \frac{32Za}{3e^{2/7}} + \left(\frac{3}{32Za} \right)^{\frac{1}{2}} A_m^{(1/6)} &= \frac{3}{28Z}, \\ \frac{1}{2} \ln \frac{2Za}{3e^2} + \frac{8a}{3\rho} \delta + \frac{4a}{\rho} A_m^{(1/6)} &= \beta + \sqrt{2} \rho^{\frac{1}{2}} B_r^{(1/2)}, \end{aligned}$$

in order to ensure the asymptotic matching in the whole domain. It is quite remarkable that the conditions that determine the coefficients arrive from the matching of secondary terms instead of the dominant ones.

After solving $A_m^{(1/6)}$ and $B_r^{(1/2)}$ from the previous set of equations, the second order solution can be built up. Indeed, two extra terms should be added to suppress the effect of the

remanent time logarithmic tails coming from the secondary terms of Eqs. (B2) and (B3). The corrections are $\mathcal{O}(t^{-1/6} \ln t)$ and $\mathcal{O}(t^{-1/2} \ln t)$, respectively, and are related to the translational invariance of the solution. This intermediate-order matching led to homogeneous equations in the rim and intermediate regions that can be solved directly.

At this point, it seems that there is not any condition for the tip position correction c_{12} at this order. However, a careful analysis of the matching conditions shows that the $\mathcal{O}(1)$ correction in Eq. (B1), γ , becomes dominant when the far-field and intermediate regions are matched. In order to annihilate this term, the first correction of the tip position should satisfy

$$c_{1/2} = \frac{3}{4} \rho \left(1 - \frac{2}{9} \pi Z \right). \tag{B4}$$

Taking all of these considerations into account, our second order asymptotical approach is finally written in terms of $z = x + 2c_{12}t^{1/2}$ and given by

$$\begin{aligned} h(z, t) &= h_f^{(0)}(z) + t^{\frac{1}{6}} h_m^{(0)}\left(zt^{-\frac{1}{6}}\right) + t^{\frac{1}{6}} h_m^{(1/6)}\left(zt^{-\frac{1}{6}}\right) + t^{\frac{1}{6}} h_r^{(0)}\left(zt^{-\frac{1}{2}}\right) + t^{\frac{1}{6}} h_r^{(1/3)}\left(zt^{-\frac{1}{2}}\right) \\ &+ h_r^{(1/2)}\left(zt^{-\frac{1}{2}}\right) - \frac{3}{32Z} z^2 + \frac{3}{28Z} z \ln z - \frac{3}{28Z} z - (2\rho)^{\frac{1}{2}} t^{\frac{1}{4}} z^{\frac{1}{2}} + A_0 \left(\frac{2Za^5}{3} \right)^{\frac{1}{4}} t^{\frac{5}{12}} z^{-\frac{1}{2}} \\ &- \frac{2Z}{3} \rho^{-1} t^{\frac{1}{2}} z^{-1} + \frac{1}{4\sqrt{2}} \rho^{\frac{1}{2}} t^{\frac{1}{4}} z^{-\frac{1}{2}} \ln z + \left(\beta + \sqrt{2} \rho^{\frac{1}{2}} B_r^{(1/2)} \right) t^{\frac{1}{4}} z^{-\frac{1}{2}} \\ &- \frac{1}{14} \left(\frac{2a}{3Z} \right)^{\frac{1}{2}} t^{\frac{1}{6}} \ln t v_m\left(zt^{-\frac{1}{6}}\right) - \frac{5}{56} \ln t w_r\left(zt^{-\frac{1}{2}}\right) - \frac{1}{56Z} \ln t z - \frac{1}{16\sqrt{\pi}} t^{\frac{1}{4}} \ln t z^{-\frac{1}{2}}. \end{aligned}$$

¹G. I. Taylor, “The dynamics of thin sheets of fluid III. Disintegration of fluid sheets,” *Proc. Roy. Soc. London A*, **253**, 313 (1959).

²F. E. C. Cullick, “Comments on a ruptured soap film,” *J. Appl. Phys.* **31**, 1128 (1960).

³J. Keller and M. Miksis, “Surface tension driven flows,” *SIAM J. Appl. Math.* **43**, 268 (1983).

⁴K. Miyamoto and Y. Katagiri, *Curtain Coating*, edited by S. Kistler and P. Schweizer (Chapman and Hall, London, 1997).

⁵N. Bremond, C. Clanet, and E. Villermaux, “Atomization of undulating liquid sheets,” *J. Fluid Mech.* **585**, 421 (2007).

⁶J. Eggers and E. Villermaux, “Physics of liquid jets,” *Rep. Prog. Phys.* **71**, 036601 (2008).

⁷M. Rein, “Phenomena of liquid drop impact on solid and liquid surfaces,” *Fluid Dyn. Res.* **12**, 61 (1993).

⁸L. Limat, P. Jenffer, B. Dagens, E. Tournon, M. Fermigier, and J. Wesfreid, “Gravitational instabilities of thin liquid layers: Dynamics of pattern selection,” *Physica D* **61**, 166 (1992).

⁹X. Hu and A. Jacobi, “The intertube falling film: Part1—flow characteristics, mode transitions and hysteresis,” *Trans. ASME, Ser. C: J. Heat Transfer* **118**, 616 (1996).

- ¹⁰E. Villermaux and C. Clanet, "Life of a flapping liquid sheet," *J. Fluid Mech.* **462**, 341 (2002).
- ¹¹C. Josserand and S. Zaleski, "Droplet splashing on a thin liquid film," *Phys. Fluids* **15**, 1650 (2003).
- ¹²L. V. Zhang, P. Brunet, J. Eggers, and R. D. Deegan, "Wavelength selection in the crown splash," *Phys. Fluids* **22**, 122105 (2010).
- ¹³E. Villermaux and B. Bossa, "Drop fragmentation on impact," *J. Fluid Mech.* **668**, 412 (2011).
- ¹⁴G. Debrégeas, P. Martin, and F. Brochard-Wyart, "Viscous bursting of suspended films," *Phys. Rev. Lett.* **75**, 3886 (1995).
- ¹⁵G. Debrégeas, P. de Gennes, and F. Brochard-Wyart, "The life and death of bare viscous bubbles," *Science* **279**, 1704 (1998).
- ¹⁶M. Brenner and D. Gueyffier, "On the bursting of viscous films," *Phys. Fluids* **11**, 737 (1999).
- ¹⁷G. Sünderhauf, H. Raschzillier, and F. Durst, "The retraction of the edge of a planar liquid sheet," *Phys. Fluids* **14**, 198 (2002).
- ¹⁸R. Krechetnikov, "Stability of liquid sheet edges," *Phys. Fluids* **22**, 092101 (2010).
- ¹⁹J. M. Fullana and S. Zaleski, "Stability of a growing end-rim in a liquid sheet of uniform thickness," *Phys. Fluids* **11**, 952 (1999).
- ²⁰I. Roisman, K. Horvat, and C. Tropea, "Spray impact: Rim transverse instability initiating fingering and splash, and description of a secondary spray," *Phys. Fluids* **18**, 102104 (2006).
- ²¹M. Song and G. Tryggvason, "The formation of thick borders on an initially stationary fluid sheet," *Phys. Fluids* **11**, 2487 (1999).
- ²²S. Popinet, *Gerris Flow Solver* (supported by the National Institute of Water and Atmospheric Research, Auckland, NZ, and Institut Jean Le Rond d'Alembert, Paris, FR, as at October 2011, available at <http://gfs.sourceforge.net/>).
- ²³S. Popinet, "Gerris: A tree-based adaptive solver for the incompressible euler equations in complex geometries," *J. Comput. Phys.* **190**, 572 (2003).
- ²⁴S. Popinet, "An accurate adaptive solver for surface-tension-driven interfacial flows," *J. Comput. Phys.* **228**, 5838 (2009).
- ²⁵G. Agbaglah, S. Delaux, D. Fuster, J. Hoepffner, C. Josserand, S. Popinet, P. Ray, R. Scardovelli, and S. Zaleski, "Parallel simulation of multiphase flows using octree adaptivity and the volume-of-fluid method," *C.R. Mécanique* **339**, 194 (2011).
- ²⁶J. Keller, A. King, and L. Ting, "Blob formation," *Phys. Fluids* **7**, 226 (1995).
- ²⁷T. Erneux and S. Davis, "Nonlinear rupture of free films," *Phys. Fluids* **5**, 1117 (1993).
- ²⁸M. V. Dyke, *Perturbation Methods in Fluid Mechanics* (The Parabolic, Stanford, CA, 1975).
- ²⁹D. Fuster, G. Agbaglah, C. Josserand, S. Popinet, and S. Zaleski, "Numerical simulation of droplets, bubbles and waves: state of the art," *Fluid Dyn. Res.* **41**, 065001 (2009).
- ³⁰É. Reyssat and D. Quéré, "Bursting of a fluid film in a viscous environment," *Europhys. Lett.* **76**, 236 (2006).
- ³¹J. B. Bostwick and P. H. Steen, "Stability of constrained cylindrical interfaces and the torus lift of Plateau-Rayleigh," *J. Fluid Mech.* **647**, 201 (2010).
- ³²P. Yecko and S. Zaleski, "Transient growth in two-phase mixing layers," *J. Fluid Mech.* **528**, 43 (2005).
- ³³T. Boeck and S. Zaleski, "Viscous versus inviscid instability of two-phase mixing layers with continuous velocity profile," *Phys. Fluids* **17**, 032106 (2005).
- ³⁴H. Lhuissier and E. Villermaux, "Soap films burst like flapping flags," *Phys. Rev. Lett.* **103**, 054501 (2009).
- ³⁵E. Villermaux and B. Bossa, "Drop fragmentation on impact," *J. Fluid Mech.* **668**, 412 (2011).